Meyer and Waas *Integrating Materials and Manufacturing Innovation* (2015) 4:5
DOI 10.1186/s40192-015-0034-z

Integrating Materials and Manufacturing Innovation
a SpringerOpen Journal

RESEARCH ARTICLE Open Access

Mesh-objective two-scale finite element analysis of damage and failure in ceramic matrix composites

Pascal Meyer and Anthony M Waas*

*Correspondence:
awaas@aa.washington.edu
Department of Aeronautics and Astronautics, University of Washington, Seattle, WA 98195 - 2400

Abstract

A mesh-objective two-scale finite element approach for analyzing damage and failure of fiber-reinforced ceramic matrix composites is presented here. The commercial finite element software suite Abaqus is used to generate macroscopic models, e.g., structural-level components or parts of ceramic matrix composites (CMCs), coupled with a second finite element code which pertains to the sub-scale at the fiber-matrix interface level, which is integrated seamlessly using user-generated subroutines and referred to as the integrated finite element method (IFEM). IFEM calculates the reaction of a microstructural sub-scale model that consists of a representative volume element (RVE) which includes all constituents of the actual material, e.g., fiber, matrix, and fiber/matrix interfaces, details of packing, and nonuniformities in properties. The energy-based crack band theory (CBT) is implemented within IFEM's sub-scale constitutive laws to predict micro-cracking in all constituents included in the model. The communication between the micro- and macro-scale is achieved through the exchange of strain, stress, and stiffness tensors. Important failure parameters, e.g., crack path and proportional limit, are part of the solution and predicted with a high level of accuracy. Numerical predictions are validated against experimental results.

Keywords: Multi-scale analysis; Crack band; Ceramic matrix composites; Finite elements

Background

Polymer matrix composites (PMCs) and ceramic matrix composites (CMCs) are increasingly used in a wide range of applications. With the demand for lighter and more versatile structural components, the need to understand interactive and complex failure mechanisms in these materials has grown and has become the focus of many research projects. The deformation response, subsequent damage development, and failure of these multi-constituent materials are dependent on microstructural details such as variations in fiber packing arrangement, properties at fiber-matrix interfaces, and interactions between neighboring fibers. This dependency of failure modes on the microstructure is well known for composite materials which led to the development of numerous homogenized theories. Kanoute et al. [1] reviewed various multi-scale methods for mechanical and thermomechanical responses of composites. Heinrich and Waas [2] utilized the smeared crack approach to describe the post-peak softening in laminated materials. They

predicted the cracking behavior of an open-hole tensile specimen and recorded crack directions for various fiber angles. Accurate numerical predictions for layered, fibrous materials are inherently difficult due to the intricate mechanisms that tie global component failure to microstructural degradation. Modeling strategies based on homogenized material properties neglect the importance of the physical behavior at the microstructural level, and thus, homogenized models fail to predict experimentally observed critical parameters accurately. Those include, e.g., maximum load, strain to failure, crack spacing, and other salient features. Oftentimes, the material orientation is used as a guide for directing failure. This might lead to erroneous crack paths for materials with similar fiber and matrix properties such as CMCs. Hence, multi-scale methods have become the focus of many research papers in recent years. These models dehomogenize the strain and stress state for each constituent. Typically, a representative volume element (RVE) that preserves the microstructural dimensions is identified. Yuan and Fish [3] developed a computational homogenization approach for linear and nonlinear solid mechanics problems. In this work, two commercial solvers were bridged by a python code. The authors showed that linear problems could be accurately modeled. Ghosh et al. [4] introduced a multi-scale methodology based on the Voronoi cell finite element method (VCFEM). Material coefficients are generated by VCFEM and used in a global finite element model. Nonlinearities can be included in the finite element formulation of the Voronoi cells. Key et al. [5] used multi-continuum technology in a multi-scale simulation to analyze the separation of rib to skin interfaces. Multi-continuum theory decomposes the stress and strain field for each constituent using volume averages. This method is numerically fast with the cost of inaccuracy particularly for components that experience high shear. Bacarreza et al. [6] developed a semi-analytical homogenization method to model damage in woven composite materials. Effective material properties are derived and used in a progressive damage analysis. Nonlocal or gradient failure theories assume that the post-peak stress-strain behavior of an element is influenced by the field gradients within a characteristic radius around the element. Jirásek [7] analyzed analytical and numerical solutions of simple one-dimensional localization problems. Aboudi et al. [8] introduced the generalized method of cells (GMC), a semi-analytical method, which discretized the microstructure with rectangular subcells. Pineda et al. [9] achieved mesh objectivity with a thermodynamics-based approach within GMC as well as high-fidelity generalized method of cells (HFGM). Multi-scaling methods often suffer from lower computational efficiency compared to homogenized models. This disadvantage can usually be overcome by using the multi-scale method in areas where microstructural failure is to be expected, e.g., at stress concentrators (notches, etc.). Homogenized element stress-strain relation can be utilized in regions of low failure probability. In recent years, significant improvements have been made in terms of fidelity and computational efficiency [10-13].

In the present paper, the commercial finite element software suite Abaqus is used to generate lamina-level structural model of a ceramic matrix composite (CMC). A second sub-scale microstructural model has been developed and fully integrated with the main Abaqus solver through a user material subroutine (UMAT). Integrated finite element method (IFEM) calculates the reaction of a microstructural model to an imposed displacement field. The microstructural model consists of a RVE which includes all constituents of the real material, e.g., fiber, matrix, and fiber/matrix interfaces, details of packing, and nonuniformities in properties. The energy-based crack band theory (CBT),

first introduced by Bažant [14], is implemented within IFEM constitutive laws to predict micro-cracking in all constituents that are included in the micromechanics model. The communication between the micro- and macro-scale is achieved through the exchange of strain, stress, and stiffness tensors. Important failure parameters, e.g., crack path and proportional limit, are part of the solution and predicted with a high level of accuracy. Numerical predictions are validated against experimental results.

Methods

Representative volume element modeling in a multi-scale framework

Most commercially available finite element suites offer the user to implement custom constitutive material laws. In this work, Abaqus has been chosen to solve the macroscopic-scale (e.g., lamina level) finite element problem. User material subroutines, called UMAT (*Abaqus User Manual* [15]), are readily accessible through the computer language Fortran. The UMAT subroutine is called at each integration point of the Abaqus model for each element within an element set that has been defined with a user material. In a multi-scale scheme, information is exchanged between multiple length and/or time scales. Here, the focus lies on a concurrent technique that exchanges essential stiffness, current stress, and strain information between two scales: the lamina-level simulation and a microstructure-level simulation. This technique employs the finite element method (FEM) at both the fiber/matrix scale and the macroscopic, e.g., lamina-level scale. The constitutive response at the macro-scale is purely dictated by the fiber/matrix-level model. Localization techniques, as discussed below and referenced in Equation 10, are employed for transforming displacement fields from a global state to a local state. Back-transformation is achieved through a homogenization step according to Equation 1. The concurrent information exchange between the scales is shown in Figure 1. A strain field is passed to the user-defined material definition. Stress and stiffness tensors are calculated and passed back to Abaqus.

In IFEM, interactions of fibers, interfaces, and matrices are captured with great detail without loosing computational efficiency. Figure 2 displays a flow chart of the implemented two-scale method. The sub-scale is being called at each material integration point of the macroscopic model. In order to reduce the computational cost, a criterion based on the homogenized strain state is used to determine if constituent failure is possible.

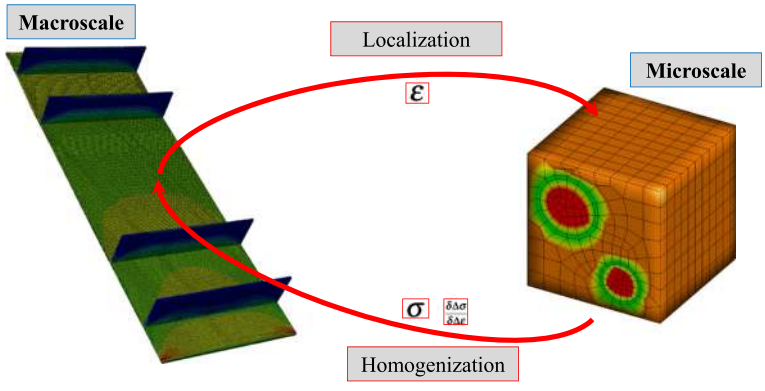

Figure 1 Multi-scale information exchange between scales.

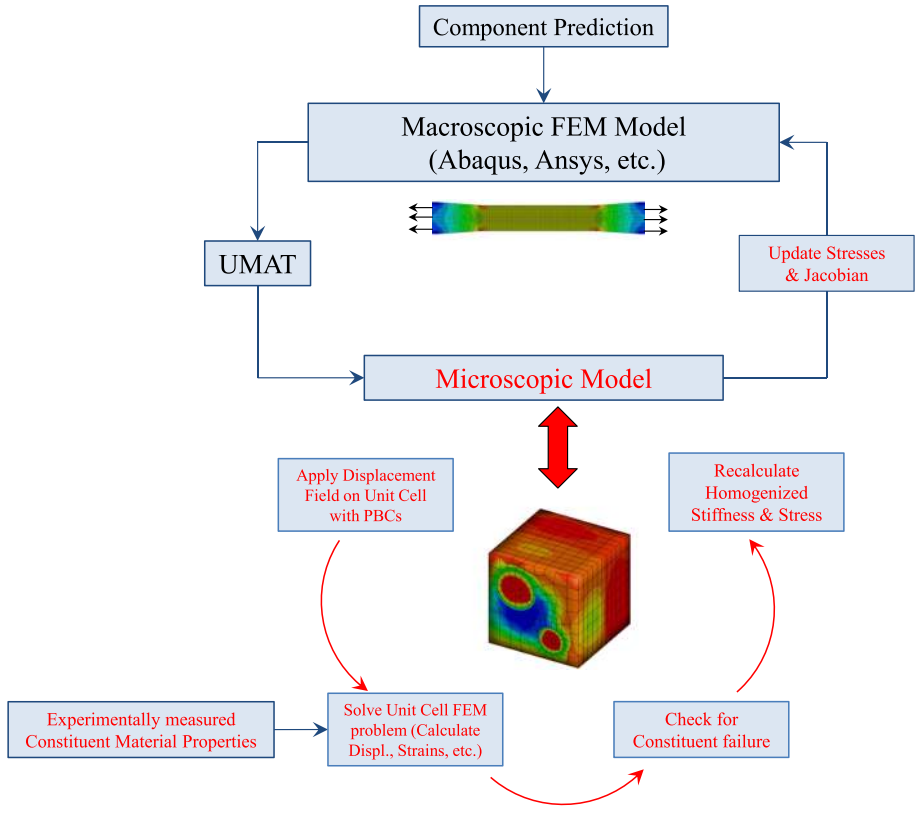

Figure 2 IFEM flow chart.

This criterion is chosen to make conservative estimates while simultaneously avoiding unnecessary calls to the sub-scale.

Four main steps can be identified within the sub-scale code. First, the element matrices are calculated and then assembled to form a global system of equations. In a second step, periodic boundary conditions (PBCs) are applied, and the global nodal displacement fields are calculated. The global solution is used in a third step to derive the required set of element strains and stresses. Finally, a failure criterion is checked for each element within the RVE, and volume averaged stresses, Equation 1, are calculated and passed back to the macro-scale in order to update the stress state of the element in the macroscopic model:

$$\sigma_{ij}^{V} = \frac{1}{V}\int \sigma_{ij}^{e}\,\mathrm{d}V \tag{1}$$

Two versions of IFEM have been developed. 3D-IFEM uses a linear eight-noded brick elements and 2D-IFEM uses a four-noded plane stress (or strain) element formulation, respectively, as can be found in [16]. This work will focus on 3D-IFEM due to an increased accuracy with minor impact on the computational cost. The equations for the three-dimensional formulation are presented. The geometry of each element is described by Cartesian coordinates (X_i, Y_i, Z_i) of the nodes. Each node i has three degrees of freedom (u_i, v_i, w_i), and the nodal degree of freedom vector $\mathbf{q}$ can be written as:

$$\{q\}^T = \{u_1, v_1, w_1, u_2, v_2, w_2, \ldots, \ldots, \ldots, u_8, v_8, w_8\} \tag{2}$$

The corresponding nodal force vector is:

$$\{f\}^T = \{f_{x1}, f_{y1}, f_{z1}, f_{x2}, f_{y2}, f_{z2}, \ldots, \ldots, \ldots, f_{x8}, f_{y8}, f_{z8}\} \tag{3}$$

The displacement components at any point (X, Y, Z) can be interpolated by the nodal displacements:

$$\{u\} = [N]\{q\} \tag{4}$$

The eight shape functions can be written as:

$$N_i = \frac{1}{8}(1 + \xi\xi_i)(1 + \zeta\zeta_i)(1 + \eta\eta_i) \tag{5}$$

The isoparametric transformation is given by:

$$\begin{aligned} x &= N_1 x_1 + N_2 x_2 + \ldots + N_8 x_8 \\ y &= N_1 y_1 + N_2 y_2 + \ldots + N_8 y_8 \\ z &= N_1 z_1 + N_2 z_2 + \ldots + N_8 z_8 \end{aligned} \tag{6}$$

Next, the Jacobian matrix of the derivative transformation from real coordinates (X, Y, Z) to isoparametric coordinates can be written as:

$$J = \begin{bmatrix} \frac{\partial x}{\partial \xi} & \frac{\partial y}{\partial \xi} & \frac{\partial z}{\partial \xi} \\ \frac{\partial x}{\partial \eta} & \frac{\partial y}{\partial \eta} & \frac{\partial z}{\partial \eta} \\ \frac{\partial x}{\partial \zeta} & \frac{\partial y}{\partial \zeta} & \frac{\partial z}{\partial \zeta} \end{bmatrix} \tag{7}$$

The stresses and strains are then given by:

$$\begin{aligned} \sigma &= [\sigma_x, \sigma_y, \sigma_z, \tau_{xy}, \tau_{xz}, \tau_{yz}]^T \\ \epsilon &= [\epsilon_x, \epsilon_y, \epsilon_z, \gamma_{xy}, \gamma_{xz}, \gamma_{yz}]^T \end{aligned} \tag{8}$$

Finally, a matrix relating the element strains and nodal displacements can be derived:

$$\{\epsilon\} = [B]\{q\} \tag{9}$$

Implementing IFEM in Fortran was essential for a highly efficient multi-scale framework. It allows the macroscopic model to be run in a cluster environment and hence solving multiple material integration points simultaneously.

Dehomogenization of displacement field with periodic boundary conditions

One essential step in these two-scale simulations is the dehomogenization of the global displacement field. Load has to be transferred at each material point of the coarse scale model to the microscopic subcell model. In this work, PBCs are used to apply the homogenized strain state at each integration point of the macroscale model on the RVE. PBCs enforce displacement continuity on all outer surface nodes of the RVE with the assumption that the RVE is part of an infinite continuum [17,18]. Equation 10 represents the

three-dimensional formulation. These equations can be easily simplified to two dimensions. For compactness, only the three-dimensional periodic boundary conditions are explicitly discussed here:

$$\begin{aligned}
u_1(L_1,x_2,x_3) - u_1(0,x_2,x_3) &= \epsilon_{11}L_1 \\
u_2(L_1,x_2,x_3) - u_2(0,x_2,x_3) &= 2\epsilon_{12}L_1 \\
u_3(L_1,x_2,x_3) - u_3(0,x_2,x_3) &= 2\epsilon_{13}L_1 \\
u_1(x_1,L_2,x_3) - u_1(x_1,0,x_3) &= 2\epsilon_{21}L_2 \\
u_2(x_1,L_2,x_3) - u_2(x_1,0,x_3) &= \epsilon_{22}L_2 \\
u_3(x_1,L_2,x_3) - u_3(x_1,0,x_3) &= 2\epsilon_{23}L_2 \\
u_1(x_1,x_2,L_3) - u_1(x_1,x_2,0) &= 2\epsilon_{31}L_3 \\
u_2(x_1,x_2,L_3) - u_2(x_1,x_2,0) &= 2\epsilon_{32}L_3 \\
u_3(x_1,x_2,L_3) - u_3(x_1,x_2,0) &= \epsilon_{33}L_3
\end{aligned} \tag{10}$$

where ϵ_{ij} are the macroscopic strains passed down from Abaqus at each integration point. L_1, L_2, and L_3 are the corresponding side lengths of the RVE in x-, y-, and z-directions as shown in Figure 3a. A sketch of the periodically deformed RVE is shown in Figure 3b.

The PBC constraints are implemented using the penalty approach:

$$\beta_1 Q_1 + \beta_2 Q_2 = \beta_0 \tag{11}$$

where Q_1 and Q_2 are the degrees of freedom (dofs) to be coupled and β_0 the applied displacement between Q_1 and Q_2. β_1 and β_2 are integer parameters with a value of 1 and -1, respectively.

Numerical calculation of Jacobian matrix for implicit simulations

All numerical predictions in this work were carried out using an implicit solution methodology in Abaqus. Due to the nature of the backward Euler scheme used in Abaqus implicit simulations, a Jacobian matrix $\delta\Delta\sigma \backslash \delta\Delta\epsilon$ has to be passed back at the end of the user-defined material law [15]. In case of the undamaged subcell, the Jacobian matrix is constant and calculated only once for each RVE prior to the multi-scale simulation. It is

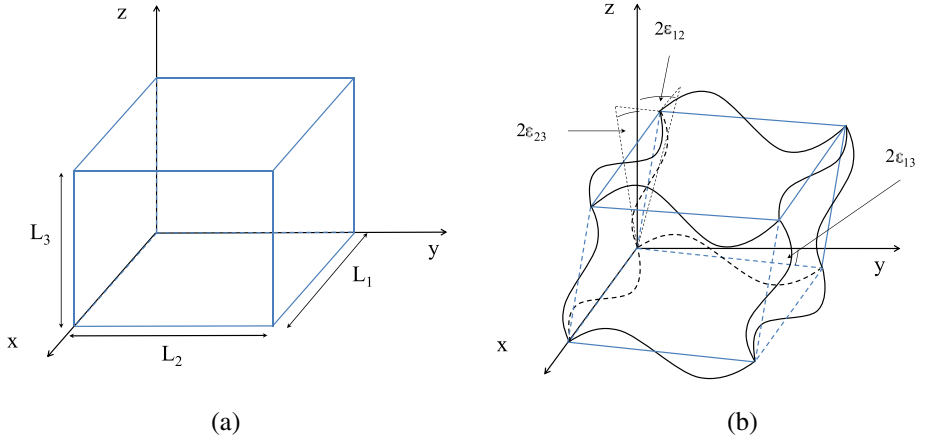

Figure 3 Periodic boundary conditions: (a) undeformed state and (b) deformed state.

stored in a Fortran-compiled file and can be called at any time during the IFEM simulation. In case of damage in the subcell model, a new Jacobian matrix should be calculated to guarantee fast convergence of the macroscopic model. It should be noted that a constant Jacobian matrix might lead to convergence but at the cost of loosing a quadratic convergence rate during the Newton-Raphson method used in the Abaqus FEM solution process. Since the sub-scale includes details of the microstructure, failure mechanisms, and interactions among these, the sub-scale generated material law to be used at the macro-scale is embedded in details of the Jacobian matrix, denoted in Abaqus UMATs as DDSDDE, and this is determined numerically:

$$\left\{\begin{matrix}\epsilon_{11}\\0\\0\\\epsilon_{12}\\0\\0\end{matrix}\right\},\left\{\begin{matrix}0\\\epsilon_{22}\\0\\0\\\epsilon_{23}\\0\end{matrix}\right\},\left\{\begin{matrix}0\\0\\\epsilon_{33}\\0\\0\\\epsilon_{13}\end{matrix}\right\} \tag{12}$$

Three separate sub-scale calculations on the damaged subcells are needed to calculate all entries of the Jacobian matrix. Therefore, three global strain vectors, Equation 12, are applied on the boundaries of the damaged subcell separately, and the corresponding stress state is determined. Equations 13 depicts the calculation of the first column of the Jacobian matrix as well as the entry S_{1212}:

$$\left\{\begin{matrix}\sigma_{11}\\\sigma_{22}\\\sigma_{33}\\\sigma_{12}\\\sigma_{23}\\\sigma_{13}\end{matrix}\right\}=\left\{\begin{matrix}S_{1111}&S_{1122}&S_{1133}0&0&0&\\S_{1122}&S_{22222}&S_{2233}0&0&0&\\S_{1133}&S_{2233}&S_{3333}0&0&0&\\0&0&0&S_{1212}&0&0\\0&0&0&0&S_{2323}&0\\0&0&0&0&0&S_{1313}\end{matrix}\right\}\left\{\begin{matrix}\epsilon_{11}\\0\\0\\\epsilon_{12}\\0\\0\end{matrix}\right\} \tag{13}$$

This scheme requires additional numerical effort on the micro-scale model but ultimately leads to a reduction of time required to solve the macroscopic finite element problem due to faster convergence of the Abaqus model.

RVE characteristics

The objective of multi-scale analyses is to decompose a general homogenized stress and strain field of a lamina-level model into constituent stress and strain states. Post-peak softening is based on these decomposed stresses and strains, and therefore, failure is dependent on geometrical features and constituent material response within the RVE. Theoretically, there are no geometrical limitations on the RVE. However, as stated earlier, the choice of RVE size and features are predicated on experimental observations that provide qualitative and quantitative insight on damage and failure mechanisms. In this research, the maximum number of fibers per RVE was limited to three. This number of fibers resulted in a runtime of several hours using 12 processors within a cluster environment. However, future work will focus on the influence of detail within a subcell on the runtime and accuracy of numerical predictions. Furthermore, the discretization size should be selected to arrive at a minimum number of degrees of freedom within the RVE. Further restrictions might be imposed by the failure models used within the sub-scale. The crack band method for example requires a minimum characteristic element length

as further discussed in the 'Crack band failure model' section. Often overlooked is the importance of microstructural details on the failure mechanisms in numerical models. Detailed views of microstructures of composite materials reveal a random organization of fibers. Perfectly hexagonal packed RVE's, as they are often used in numerical models due to the simple architecture, can merely be an approximation. Many different deviations of the perfect packing are found in real materials, e.g., fiber touching and varying fiber diameters. Multi-scale methods are well suited to implement a random microstructure by using several RVE's with varying architectures randomly distributed throughout the macroscopic model. Hence, each element within the macroscopic model will use a RVE that slightly differs from the neighboring RVEs. Figure 4 shows examples of six geometrically different three-dimensional three-phase (fiber, matrix, interface) RVEs. It should be noted for completeness that material properties (critical stress, toughness, etc.) can also exhibit spatial variations in a deterministic or random manner. Uniform properties are assumed in this preliminary study, and other cases will be addressed in the future.

The choice of the three-phase RVEs, including fiber, interface, and matrix, created to represent the microstructure of ceramic matrix composites (CMCs) is based on observations from experiment; however, the approach developed here is not limited to these types of materials. Two-phase (polymer matrix composites) or one-phase material (pure matrix) RVEs for example are possible and can be used. The objective here is to demonstrate that RVE features are an integral part of developing physics-based multi-scale strategies that fall within the realm of predictive science.

Crack band failure model

SiC/SiC ceramic matrix composites [19] show large deviation from linear stress-strain relation in monotonic tensile tests. This strain softening is the result of formation of micro-cracks in the matrix material. Many techniques have been used by authors in the past to capture strain softening. The smeared crack approach has been used by Heinrich and Waas [2] to predict cracking of polymer matrix composites (PMC). Pineda et al. [9] used the crack band method in a multi-scale scheme. In another work, Pineda and Waas [20] used the enhanced Schapery theory to predict damage in PMC laminates. In this paper, we restrict attention to mode I cracks, occuring at the sub-scale, i.e., cracks (straight or curved) which have no shear stress at their front. This is motivated from the

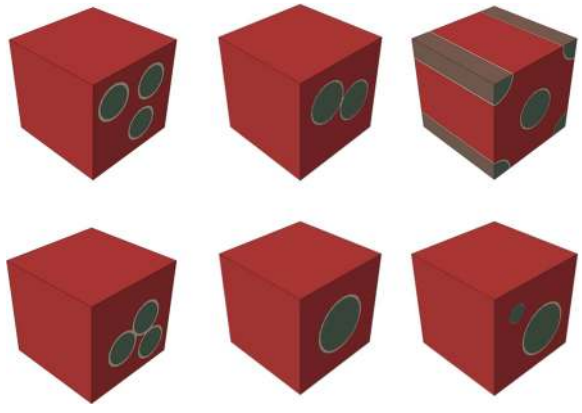

Figure 4 Selection of three-dimensional RVEs.

fact the ceramics undergo failure in a locally mode I state. This does not detract much from practical usefulness since cracks in CMCs seem to propagate in most situations along principle strain directions in which mode I prevails at the front. In finite element analysis, loss of positive definiteness of the tangent stiffness tensor leads to a material instability, which manifests as a localization of damage into the smallest length scale in the continuum problem [21]. Damage initiation, e.g., entering the traction-separation law, is based on a simple but physical criterion:

$$\frac{\epsilon'}{\epsilon_{\text{cr}}} = 1 \tag{14}$$

where ϵ' is the maximum principle strain and ϵ_{cr} is the strain to failure of the material and assumed to be a material parameter. The crack band failure method falls into the category of approaches that smear the effect of a sharp crack over a finite volume, leading to a practically useful, yet robust approach to preserve mesh objectivity. This is because the characteristic material length is embedded within the formulation of the crack band model. Thus, cracks are not explicitly modeled within an element but rather incorporated in the element constitutive law. In this work, it is assumed that after crack growth has been initiated the stiffness of the element is reduced according to a traction separation law that dissipates energy while preserving the energy release rate. In most numerical applications, the current secant stiffness is chosen such that the tractions will follow the details of the traction-separation law shown in Figure 5, where σ is the normal traction and δ is the crack opening. In this study, a triangular traction-separation law is employed. The area under the mode I traction-separation law corresponds to the mode I fracture toughness (G_{IC}) of the material, while the energy release rate G_I is defined as:

$$G_I = \int_0^{\delta} \sigma(\delta) d\delta \tag{15}$$

Objectivity with respect to the discretization size of the microscale model is achieved through introduction of a characteristic element length as further discussed in this section. It is assumed that the element strain can be written as:

$$\epsilon = \epsilon_{\text{cont}} + \epsilon_{\text{cr}} \tag{16}$$

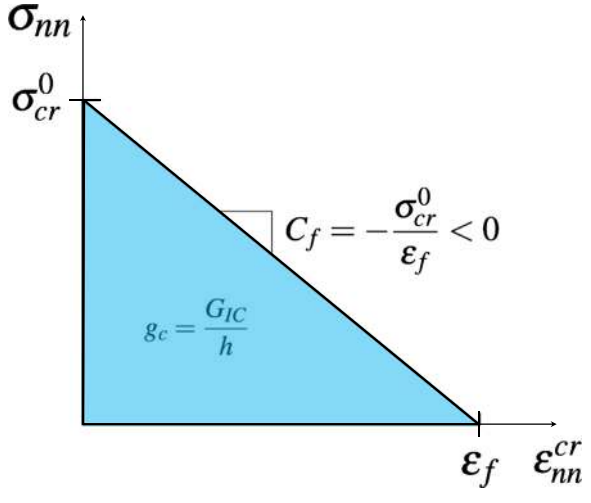

Figure 5 Crack band traction separation law.

where ϵ_{cont} represents the continuum strain of the element and ϵ_{cr} represents the additional smeared strain which results due to cracking. One can rewrite Equation 16 for a linear elastic isotropic material in the principal frame as:

$$\begin{Bmatrix} \epsilon_{11} \\ \epsilon_{22} \\ \epsilon_{33} \end{Bmatrix} = \begin{bmatrix} \frac{1}{E} & \frac{-\nu}{E} & \frac{-\nu}{E} \\ \frac{-\nu}{E} & \frac{1}{E} & \frac{-\nu}{E} \\ \frac{-\nu}{E} & \frac{-\nu}{E} & \frac{1}{E} \end{bmatrix} \begin{Bmatrix} \sigma_{11} \\ \sigma_{22} \\ \sigma_{33} \end{Bmatrix} + \begin{Bmatrix} \epsilon_{nn}^{\text{cr}} \\ 0 \\ 0 \end{Bmatrix} \tag{17}$$

It is assumed that the continuum part and the crack part are in an iso-stress state which leads to:

$$\sigma_{nn} = \sigma_{11} \tag{18}$$

The crack strain can be calculated from the traction-separation law (Figure 5):

$$\epsilon_{nn}^{\text{cr}} = \epsilon_F + \frac{\sigma 11}{C_f} \tag{19}$$

Substituting Equation 19 into Equation 17 leads to:

$$\begin{Bmatrix} \epsilon_{11} - \epsilon_f \\ \epsilon_{22} \\ \epsilon_{33} \end{Bmatrix} = \begin{bmatrix} \frac{1}{E} + \frac{1}{C_f} & \frac{-\nu}{E} & \frac{-\nu}{E} \\ \frac{-\nu}{E} & \frac{1}{E} & \frac{-\nu}{E} \\ \frac{-\nu}{E} & \frac{-\nu}{E} & \frac{1}{E} \end{bmatrix} \begin{Bmatrix} \sigma_{11} \\ \sigma_{22} \\ \sigma_{33} \end{Bmatrix} + \begin{Bmatrix} \epsilon_{nn}^{\text{cr}} \\ 0 \\ 0 \end{Bmatrix} \tag{20}$$

Next, the element continuum stress-strain relation can be coupled to the traction-separation law as shown in Figure 6. σ_{11} and ϵ_{11} are written in the local crack coordinate system. E denotes the undamaged Young's modulus in the principle frame. A fracture scalar variable D ($0 \leq D \leq 1$) is introduced which corresponds to zero if damage has not initiated. D is set to one if ϵ_{11} exceeds ϵ_f, when the element has failed catastrophically and no load can be transferred normal to the crack direction.

The total stress-strain law in the principal frame can be rewritten as:

$$\begin{Bmatrix} \epsilon_{11} - \epsilon_f \\ \epsilon_{22} \\ \epsilon_{33} \end{Bmatrix} = \begin{bmatrix} \frac{1}{(1-D)E} & \frac{-\nu}{E} & \frac{-\nu}{E} \\ \frac{-\nu}{E} & \frac{1}{E} & \frac{-\nu}{E} \\ \frac{-\nu}{E} & \frac{-\nu}{E} & \frac{1}{E} \end{bmatrix} \begin{Bmatrix} \sigma_{11} \\ \sigma_{22} \\ \sigma_{33} \end{Bmatrix} \tag{21}$$

The damage parameter D can be determined from the stress-strain relation in Figure 6:

$$E_t = \frac{\sigma_{\text{cr}}^0}{\epsilon_0 - \epsilon_f} \tag{22}$$

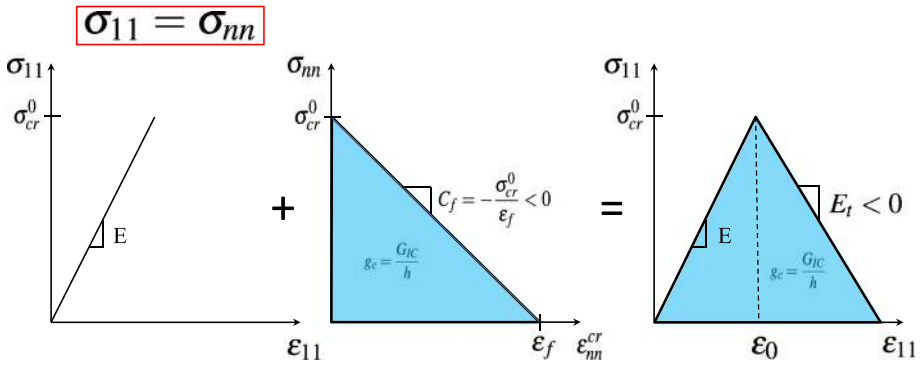

Figure 6 Joining element continuum stress-strain law with traction-separation law.

and

$$(1-D)E = \frac{E_t(\epsilon_{11}-\epsilon_f)}{\epsilon_{11}} \tag{23}$$

Using Equations 22 and 23, the scalar fracture variable D can be calculated as:

$$D = 1 - \frac{\sigma^0_{\mathrm{cr}}}{(\epsilon_f - \epsilon_0 E)}\left(\frac{\epsilon_f}{\epsilon_{11}} - 1\right) \tag{24}$$

It is assumed that damage is isotropic, which results in a compliance matrix given by Equation 25:

$$[S] = \frac{1}{(1-D)}\begin{bmatrix} S_{1111} & S_{1122} & S_{1133} & 0 & 0 & 0 \\ S_{1122} & S_{22222} & S_{2233} & 0 & 0 & 0 \\ S_{1133} & S_{2233} & S_{3333} & 0 & 0 & 0 \\ 0 & 0 & 0 & S_{2323} & 0 & 0 \\ 0 & 0 & 0 & 0 & S_{1313} & 0 \\ 0 & 0 & 0 & 0 & 0 & S_{1212} \end{bmatrix} \tag{25}$$

Finally, the compliance matrix has to be transformed back into the global x-, y-, z-coordinate system:

$$[S] = [T]^{-1}[S][T^T]^{-1} \tag{26}$$

where T is given as

$$T = [n_1 n_2 n_3][e_1 e_2 e_3] \tag{27}$$

where n_1, n_2, n_3 are the principal strain directions and e_1, e_2, e_3 are the unit basis vectors.

Characteristic length scale

In this work, the term mesh-objective prediction is used only in terms of the microscopic IFEM RVE model. Multi-scale formulations deal with several length scales. In this paper, which considers a two-scale approach, microscopic and macroscopic characteristic lengths are required. Additional work is required to incorporate the macroscopic length scale into the multi-scale formulation. Research in this area have been reported by Pineda et al. [22] who used the generalized method of cells at the sub-scale of a multi-scale analysis. FEM models that predict post-peak material softening behavior due to damage, e.g., non-recoverable energy dissipation, are inherently dependent on the discretization size of the model. In order to overcome this dependence, Bažant [14] introduced a characteristic length based on material elastic and fracture properties. In this study, the released energy is scaled by a characteristic element length, h, which is the length over which the crack opening is 'smeared' in order to define the effective strain due to cracking, as shown in Figure 6. Independent of the element size, the critical energy release rate, G_{IC}, which is assumed to be a material constant associated with damage in a particular finite element needs to be preserved. Satisfying the restriction of the mesh size guaranties a mesh-objective simulation. As can be seen in Figure 6, the strain softening modulus E_t must be negative. Therefore, the following equation holds true:

$$\frac{1}{E_t} = \frac{1}{E} + \frac{1}{C_f} \leq 0 \tag{28}$$

C_f can be replaced by $\sigma_{\text{cr}}^0/\epsilon f$, and thus, Equation 28 can be rewritten as:

$$\frac{1}{E} - \frac{2G_{IC}}{h\sigma_{\text{cr}}^2} \leq 0 \tag{29}$$

This condition leads to a maximum characteristic finite element length of:

$$h \leq \frac{2EG_{IC}}{\sigma_{\text{cr}}^2} \tag{30}$$

As Bažant [14] noted, h should be smaller but at least half of that value in practical FEM problems. The limiting case is given by $E_t^{-1} = 0$ which corresponds to a sudden drop in the stress-strain response. Since h is the distance within the element that is perpendicular to the cracking due to damage, the effective post-peak response of different element sizes will be different, yet G_{IC} is held fixed, leading to a mesh-objective formulation.

Results and discussion

Notched CMC tension simulation

Laminated ceramic matrix composites are of increasing interest especially in the aerospace and energy sector. In contrast to other materials, they experience small degradation of stiffness at very high temperatures. It should be noted that with matrix and fiber elastic properties being similar the failure mechanisms are vastly different compared to polymer matrix composites. However, 3D-IFEM is well suited to predict damage, e.g., crack paths at the macroscopic level. This will be shown for a cross-ply single-notch tension simulation. The notch radius is chosen to be large compared to the fiber diameters. The lay-up is $[0/90]_{2S}$ and model details are given in Figure 7. The gauge section width is 10.16 mm, the grip section width is 12.7 mm, and the overall length is 152.4 mm.

It further shows the boundary conditions and loading on the model. The edges X_0 and X_1 are subjected to a displacement in negative and positive x-direction, respectively. The corner A at X_0 is prevented from moving in the y- and z-directions to avoid rigid body movements. All models were meshed with three-dimensional elements (C3D8 Abaqus

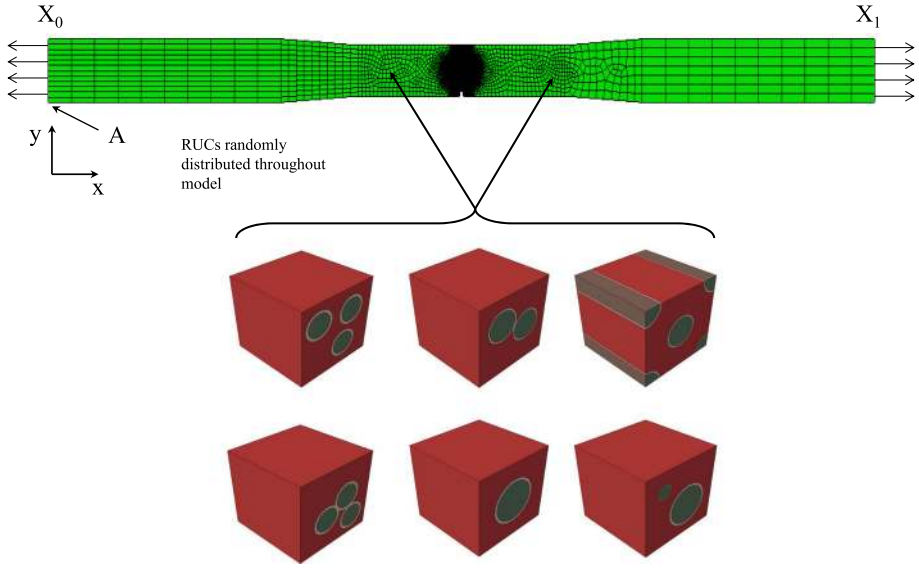

Figure 7 Cross-ply laminate model details.

v6.11 [15]) with one element per layer through the thickness. Important to note here is that like any real specimen no strict symmetry in geometry with respect to the center line of the notch exists which leads to unsymmetric failure as described below. In order to break symmetry in the model, six geometrically different RVEs were randomly distributed throughout the model. The RVEs include one, two, or three fibers each. One RVE was modeled with touching fibers. Although the RVEs are comparable in elastic properties, e.g., pre-peak behavior, differences exist for the post-peak regime. RVEs with clustering fibers exhibit higher stress concentrations and tend to initiate damage at a lower load stage compared to other RVEs.

Damage was predicted with the crack band method on the RVE scale. The coupon level failure matches with crack growth observed with digital image correlation (DIC) data as can be seen from Figure 8. Two cracks initiate at the notch tip and progress outward. Initially, the cracks grow under an angle particular for each lay-up before turning perpendicular to the loading direction. The initial angle appears to be determined by the maximum principle strain directions. Eventually, one crack path will grow faster which then determines the catastrophic failure path of the specimen. This type of crack path would not be captured with a symmetric model, e.g., symmetric mesh and no geometric randomness, since there is no numerical preference for one crack to advance more quickly. As mentioned before, finite element methods that include energy dissipation through damage will be mesh dependent if not properly treated. The crack band methodology, as currently implemented within IFEM, incorporates a characteristic length within the RVE model. However, on the macroscopic scale, such a development is absent. Three model discretization sizes at the macroscale (Figure 9) were created to study the effect on the stress-strain response of the single-edge-notch predictions. The coarse mesh (Figure 9a) consisted of 37,140 dofs, the fine mesh consisted of 110,260 dofs, and the fine structured mesh consisted of 269,835 dofs. All models were run in a cluster environment on a single node with 12 processors. Figure 10 shows the normalized stress-strain

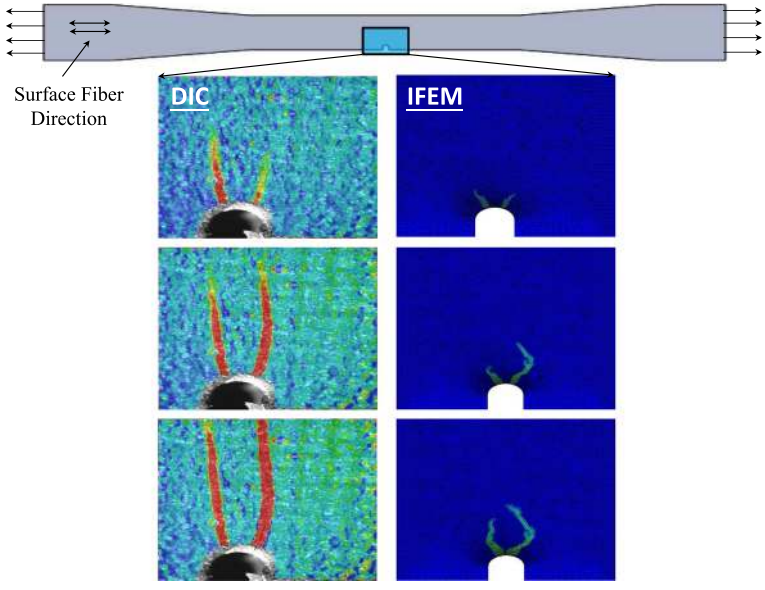

Figure 8 Comparison of crack paths of 3D-IFEM and DIC.

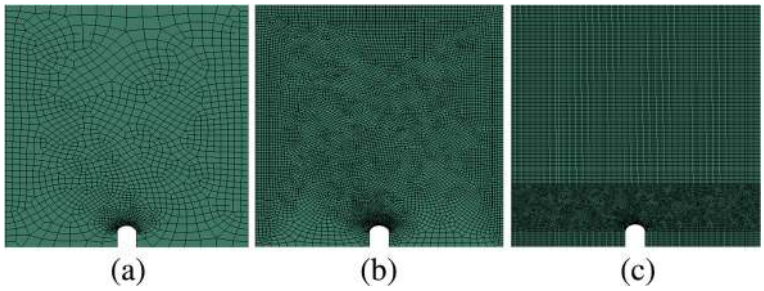

Figure 9 Three meshes of the single-edge-notch finite element model were investigated for the mesh convergence study. **(a)** Coarse mesh, **(b)**, fine mesh, and **(c)** fine structured mesh. The field of view was restricted to the area around the notch in order to resolve the mesh details.

response of all three models. The normalized ultimate net section stress decreases by 3% from 0.98 predicted with the coarse mesh (Figure 9a) to 0.95 as predicted by the discretization size used in mesh III (Figure 9c). The normalized strain at ultimate stress changes by 3.1% from 1.046 predicted with mesh I to 1.079 as predicted by the fine structured mesh.

Next, results from a uni-directional zero-degree single-layer laminate simulation are compared to experimental results. The sample was 21.65 mm long, 6.35 mm wide, and 0.38 mm thick with the notch dimensions given in Figure 11.

The model consisted of 47,564 dofs. Three-dimensional elements with reduced integration points were used (C3D8R) with one element through the thickness. The edges X_0 and X_1 are subjected to a displacement in negative and positive x-direction, respectively. Similar to the results from a cross-ply laminate, two cracks initiate at the notch. However, the angle spanned between the cracks is larger. These predictions are very consistent

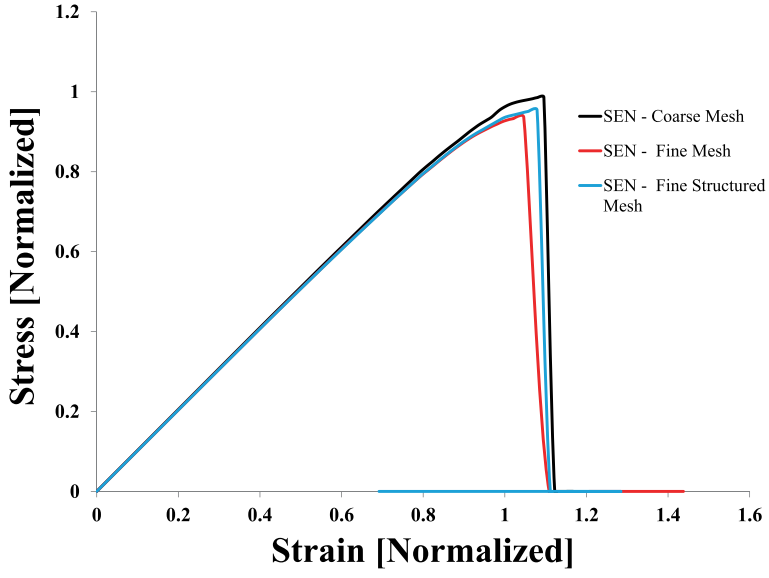

Figure 10 Stress-strain response of three model discretization sizes.

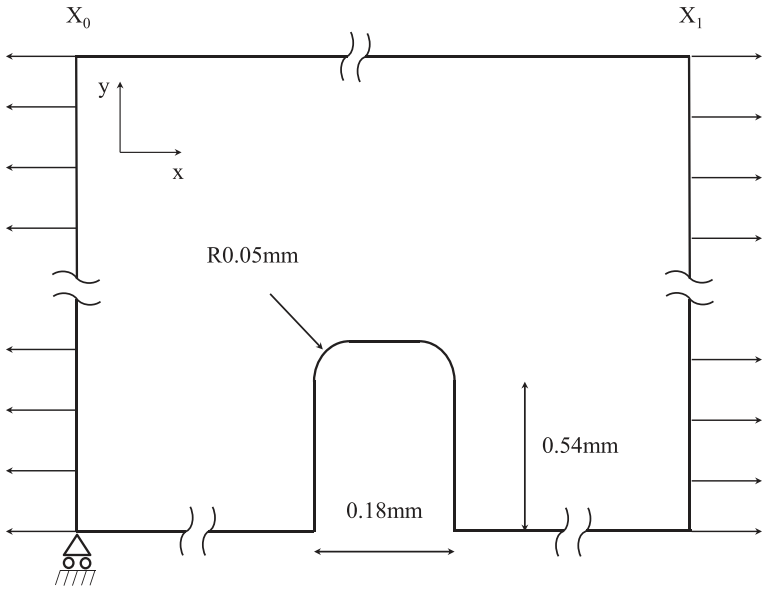

Figure 11 Sketch of unidirectional notched model.

with experimental observations shown in Figure 12. Comparable to the cross-ply laminate, the cracks turn perpendicular to the loading direction further away from the notch. Eventually, one crack propagates faster which defines the final crack path.

For both laminates, crack initiation and propagation were predicted accurately. No change to the input of the IFEM model was required. This demonstrates the strength of the IFEM two-scale approach. The fact that the experimentally observed physical behavior is accurately captured with sufficient detail at the sub-scale model lends confidence to its use for predictive studies.

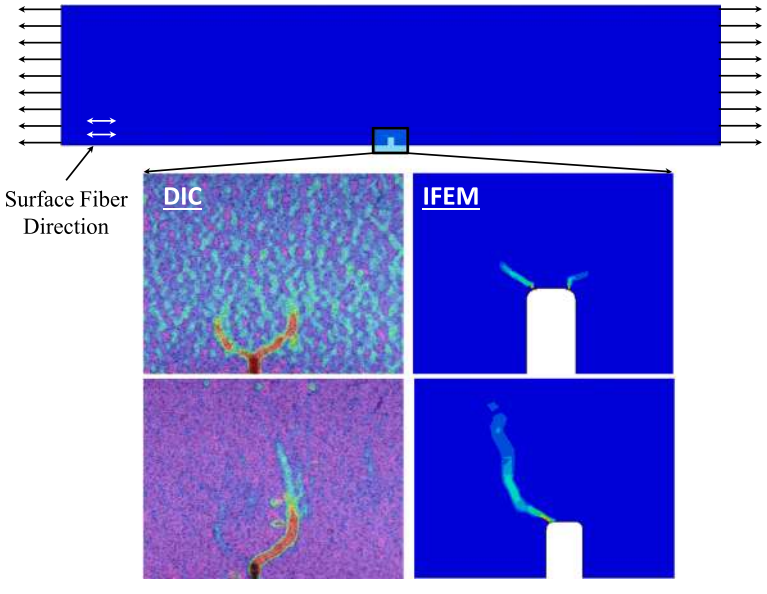

Figure 12 Damage of zero-layer laminate.

Smooth bar CMC tension simulation

In this section, 3D-IFEM will be used to analyze the failure of an eight-layer ($[0/90]_{2S}$) cross-ply smooth bar ceramic matrix composite specimen. The specimen was 152.4 mm long, 10.16 mm wide at the gauge section, and 12.7 mm wide at the grip section. Figure 13 depicts the boundary conditions. The left vertical edge was simply supported with a displacement restriction in the x-direction. The right edge was displaced in the x-direction by 0.1 mm. As before, nine randomly distributed RVEs containing five fibers each were used in order to more accurately represent the real microstructure. Three of these RVEs contained touching fibers which is often observed in this type of CMCs.

The stress-strain responses for both the numerical prediction and experimental result is shown in Figure 14. The stress and strain axes are normalized by its maximum value, respectively. The strain corresponds to the accumulated strain over the gauge section and was measured using an extensometer. It can be seen that the onset of nonlinearity in the simulation appears to be more abrupt. This might be a result of small residual stresses still present in the real specimen. In an effort to minimize the effects of residual stresses in the experiment, the specimens were heat treated before testing. The overall response predicted with 3D-IFEM is in good agreement with the experimental results. No distinctive cracks are observed at the lamina level due to the lack of geometric stress concentrations. Generally, impurities can be found in ceramic materials resulting in local changes of the matrix strength or fracture toughness. Future work will include property-based randomization and its effect on damage and failure predictions.

Conclusions

In this work, a two-scale finite element approach has been developed and fully integrated within Abaqus' user material subroutine. This enables a computationally efficient tie between a component-level model to a fiber/matrix-level model. It is shown that information exchange between these two scales through stiffness and stress transfers can capture damage on the structural-level model with effects of failure, damage, and mechanism interaction, implemented on the fiber/matrix-level model. A crack band model for the 3D-IFEM method has been developed. Numerical predictions were verified against experimental results. Good agreement was achieved for notched tensile specimens and smooth bar fibrous ceramic matrix composites. The predicted failure modes obtained with 3D-IFEM matched well with physical failure modes observed from experiments.

It was shown that the proposed failure scheme is well suited in a multi-scale framework to model progressive failure. Mesh objectivity on the RVE scale was achieved through

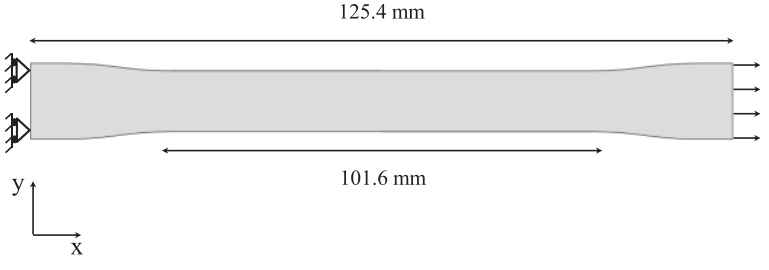

Figure 13 Simulation details of CMC smooth bar tension model.

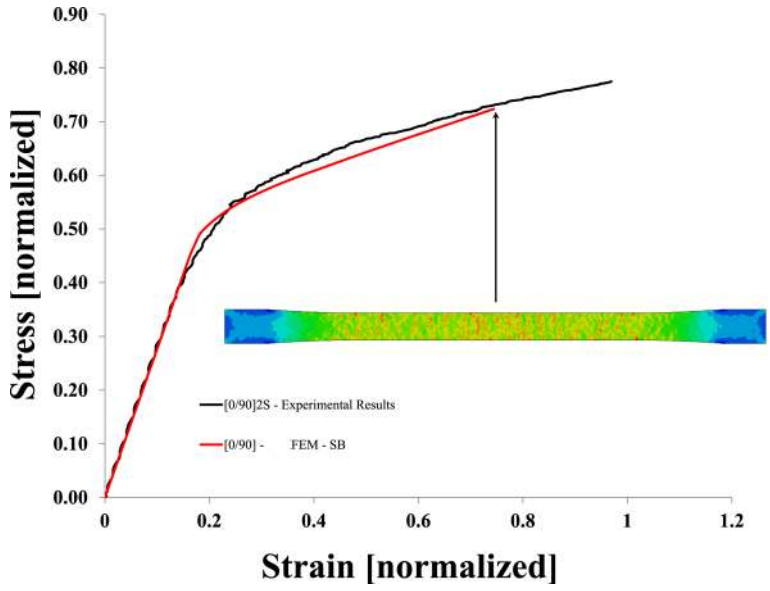

Figure 14 Normalized stress-strain response of a CMC smooth bar tension test and 3D-IFEM calculations.

introduction of a characteristic element length. Effects of anomalies of the fiber packing were captured by resolving stress and strain fields for each constituent and using randomly distributed RVEs throughout the lamina-level model. Nonsymmetric failure modes as shown for the notched specimen were predicted accurately with this technique. However, future work should more rigorously study the effect of property-based 'randomness', e.g., varying matrix strength and fracture toughness within a RVE. This effect could be most important for CMC specimens which lack a geometric stress concentration. Future work should also include a study on the effects of the amount of detail included in a RVE. Multi-scale methods need to find a healthy mean between details included in a RVE, time required to execute a simulation and accuracy of the predicted failure modes.

Competing interests
The authors declare that they have no competing interests.

Authors' contributions
PM was responsible for the implementation of the user subroutines and carried out the numerical predictions. AMW participated in developing the theoretical tools and in the study coordination. Both authors read and approved the final manuscript.

Acknowledgements
The authors are grateful to the Aerospace Engineering Department at the University of Michigan for the continued support of the research studies presented here.

Received: 14 December 2014 Accepted: 3 March 2015
Published online: 26 March 2015

References

1. Kanoute P, Boso DP, Chaboche JL, Schrefler BA (2009) Multiscale methods for composites: a review. Arch Comput Methods Eng 16:31–75
2. Heinrich C, Waas AM (2013) Investigation of progressive damage and fracture in laminated composites using the smeared crack approach. CMC-Computers Mater Continua 35:155–181
3. Yuan Z, Fish J (2008) Towards realization of computational homogenization in practice. IJNME 73:361–380
4. Ghosh S, Kyunghoon L, Moorthy S (1995) Multiple scale analysis of heterogeneous elastic structures using homogenization theory and voronoi cell finite element method. Int J Solids Struct 32:27–62

5. Key CT, Garnich MR, Hansen AC (2004) Progressive failure predictions for rib-stiffened panels based on multicontinuum technology. Composite Struct 65:357–366
6. Bacarreza O, Aliabadi MH, Apicella A (2012) Multi-scale failure analysis of plain-woven composites. J Strain Anal 47:379–388
7. Jirásek M (1998) Nonlocal models for damage and fracture: comparison of approaches. Int J Solids Struct 35:4133–4145
8. Aboudi J, Pindera MJ, Arnold SM (2001) Linear thermoelastic higher-order theory for periodic multiphase materials. J Appl Mech 68:697–707
9. Pineda EJ, Bednarcyk BA, Waas AM, Arnold SM (2013) Progressive failure of a unidirectional fiber-reinforced composite using the method of cells: discretization objective computational results. IJSS 50:1203–1216
10. Feyel F, Chaboche JL (2000) Fe^2 multiscale approach for modelling the elastoviscoplastic behaviour of long fibre SiC/Ti composite materials. Comput Methods Appl Mech Eng 183:309–330
11. Ladevèze P, Nouy A (2003) On a multiscale computational strategy with time and space homogenization for structural mechanics. Comput Methods Appl Mech Eng 192:3061–3087
12. Michel JC, Moulinec H, Suquet P (1999) Effective properties of composite materials with periodic microstructure: a computational approach. Comput Methods Appl Mech Eng 172:109–143
13. Smit RJM, Brekelmans WAM, Meijer JEH (1998) Prediction of the mechanical behavior of nonlinear heterogeneous systems by multi-level finite element modeling. Comput Methods Appl Mech Eng 155:181–192
14. Bažant ZP (1983) Crack band theory for fracture of concrete. Mater Struct 16:155–177
15. Abaqus (2008) Abaqus User's Manual. Dassault Systèmes Simulia Corp, Providence, RI. version 6.11 edition
16. Chandrupatla TR, Belegundu AD (2002) Introduction to finite elements in engineering. Pearson Education Inc., Upper Saddle River, NJ
17. Heinrich C, Aldridge M, Kieffer J, Waas AM, Shahwan K (2012) The influence of the representative volume element (RVE) size on the homogenized response of cured fiber composites. Model Simul Mater Sci Eng 20. doi:10.1088/0965-0393/20/7/075007
18. Xia Z, Zhang Y, Ellyin F (2003) A unified periodical boundary conditions for representative volume elements of composites and applications. Int J Solids Struct 40:1907–1921
19. Corman GS, Luthra KL (2005) Silicon melt infiltrated ceramic composites (HiPerComp). In: Handbook of ceramic composites. Kluwer Academic Publisher, Boston, MA. pp 99–115
20. Pineda EJ, Waas AM (2012) Modelling progressive failure of fibre reinforced laminated composites: mesh objective calculations. Aeronaut J 116:1221–1246
21. Bažant ZP, Cedolin L (1991) Stability of structures: elastic, inelastic, fracture and damage theories. Oxford University Press, New York
22. Pineda EJ, Bednarcyk BA, Waas AM, Arnold SM (2013) On multiscale modeling using the generalized method of cells: preserving energy dissipation across disparate length scales. Comput Mater Continua 35:119–154